10.1098/rspa.2001.0891

In situ observations of non-equilibrium austenite formation during weld solidification of an Fe–C–Al–Mn low-alloy steel

By S. S. Babu[1], J. W. Elmer[2], S. A. David[1] and M. A. Quintana[3]

[1] *Oak Ridge National Laboratory, Oak Ridge, TN 37831, USA*
[2] *Lawrence Livermore National Laboratory, Livermore, CA 94550, USA*
[3] *The Lincoln Electric Company, Cleveland, OH 44117, USA*

Received 7 March 2001; accepted 11 July 2001

The microstructure and properties of a welded alloy are influenced by the combined effects of solidification and subsequent solid-state transformations that occur during weld cooling. These phase transformations are further influenced by the cooling rate that the weld experiences and thus by the type of welding process that is used. In this research, microstructure development of a low-alloy steel weld was investigated under the high cooling rates produced by stationary arc welds. These welding conditions are different from the slow weld-cooling conditions, where δ-ferrite forms as the primary solidification phase. The cooling rates of the stationary welds used in this study were of the order of $10^3\,\mathrm{K\,s^{-1}}$, which were high enough to induce the formation of the non-equilibrium austenite phase during solidification. This non-equilibrium mode of solidification was directly observed using an *in situ* time-resolved X-ray diffraction technique using synchrotron radiation, and the resulting microstructures were examined using optical microscopy.

Keywords: non-equilibrium solidification; phase transformations; *in situ* synchrotron diffraction; welding process

1. Introduction

Welding processes use a variety of heat sources (arc, electron beam, laser beam and resistance heating) for joining materials. The properties of welded structures are controlled by the microstructures that evolve during interactions between the heat source and the material. For example, in steels, these interactions lead to different rates of phase equilibrium between the face-centred cubic (FCC) austenite phase and body-centred cubic (BCC) ferrite phases in both the fusion zone (FZ) and the heat-affected zone (HAZ). It is important to note that all of these changes occur over a range of time-scales, depending upon the welding process and process parameters. For example, during arc welding, with a moving heat source, the cooling rates during solidification are of the order of 1 to $10^2\,\mathrm{K\,s^{-1}}$. In contrast, the cooling rates in laser and electron-beam welding processes can reach values as high as $10^6\,\mathrm{K\,s^{-1}}$. Given the wide range of cooling rates that occur during the solidification of steel welds, it is possible that the first solid phase to form is not the one that is expected under equilibrium conditions.

 © 2002 The Royal Society

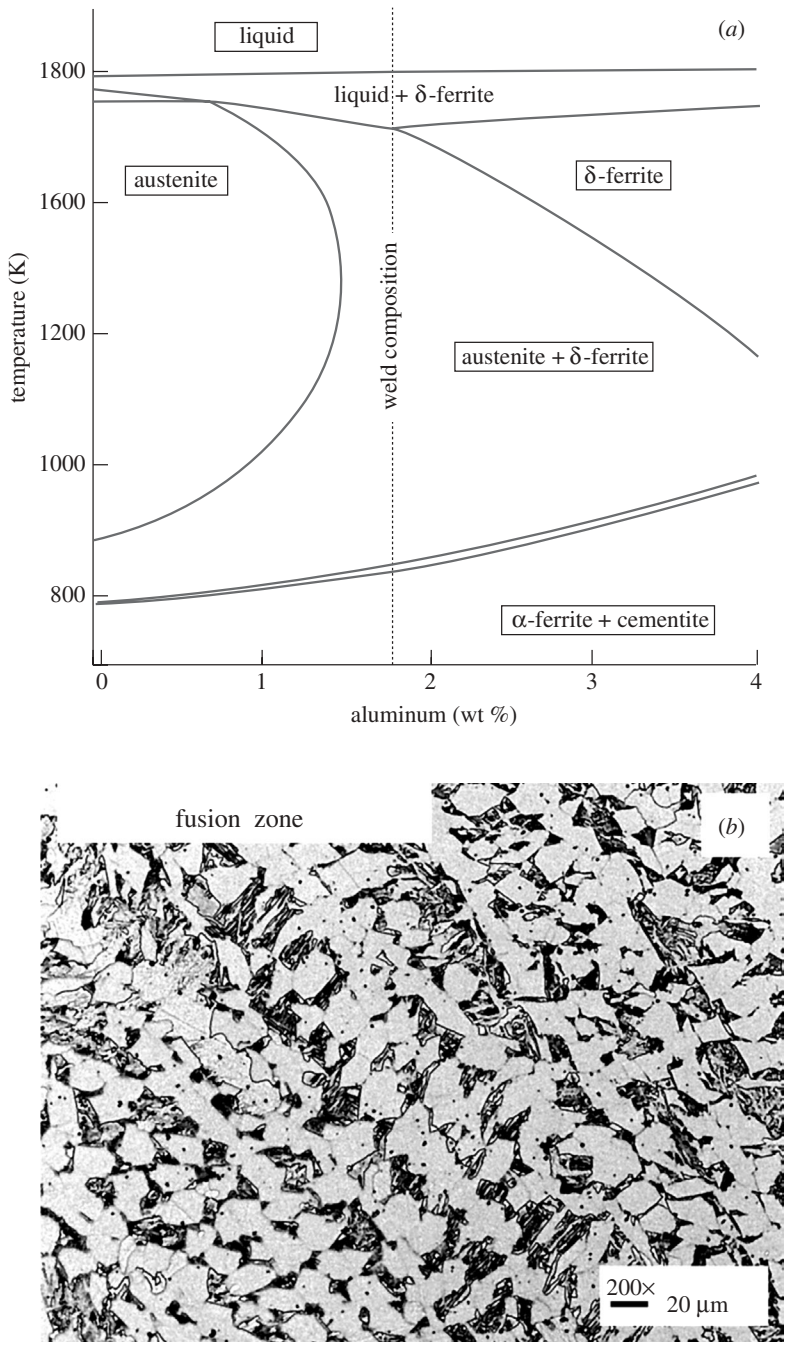

Figure 1. (*a*) Calculated equilibrium phase diagram for a steel composition (Fe–0.23 C–0.56 Mn–0.26 Si (wt %)) showing the phase stability at different temperatures as a function of aluminium concentration. (*b*) Microstructure of low-alloy steel fusion zone region (Fe–0.23 C–0.56 Mn–0.26 Si–1.77 Al–0.003 Ti–0.006 O–0.064 N (wt %)) under normal weld-cooling conditions showing skeletal δ-ferrite microstructure.

The present work addresses this issue by using time-resolved X-ray diffraction (TRXRD) to investigate phase transitions and microstructural evolution during solidification and cooling. The low-alloy steel weld used in this investigation had the following composition (Quintana *et al.* 2001): Fe–0.23 C–0.56 Mn–0.26 Si–1.77 Al–0.003 Ti–0.006 O–0.064 N (wt %). The large aluminium concentration serves to limit the ingress of oxygen and nitrogen into the weld metal. Microstructural evolution in this alloy system can be modelled using a combination of thermodynamic and kinetic methods, which predict the primary solidification phase to be δ-ferrite (Babu *et al.* 2001). An equilibrium phase diagram calculated for the weld composition using ThermoCalc® software (Sundman *et al.* 1985) is shown in figure 1*a*. As per this phase diagram, under slow cooling rates experienced during arc welding (1 to 10^2 K s^{-1}), the steel examined in this investigation is expected to solidify predominantly as δ-ferrite (Quintana *et al.* 2001). After solidification and during subsequent cooling, the δ-ferrite may partly transform to austenite, and, on further cooling, this austenite transforms to the low-temperature α-ferrite phase. This sequence of phase transitions leads to a complex microstructure, where the δ-ferrite that forms in the high temperature may be retained at room temperature. The experimental weld microstructure obtained during normal weld-cooling conditions (1 to 10^2 K s^{-1}) is shown in figure 1*b*. The microstructure shows a skeletal δ-ferrite network with transformed austenite in between these networks.

Previous research on solidification during rapid weld cooling in other steels and alloys involved *ex situ* microscopic analysis to interpret the evolution of weld microstructures (Elmer *et al.* 1989; David *et al.* 1987; Suutala 1983). Recent advances in non-equilibrium solidification theories under rapid weld cooling have also been based on the *ex situ* analyses of weld microstructures (Fukumoto & Kurz 1997, 1999; Hunziker *et al.* 1998; Boettinger *et al.* 2000). It would be useful to supplement the above indirect studies with a direct determination of phases that are present during weld solidification using *in situ* analyses. In addition, since the HAZ acts as a substrate for epitaxial growth of solid during solidification of the FZ (David & Vitek 1989), it is necessary to identify the high-temperature phases in the HAZ and their role during solidification. It is important to note that any direct measurement must be capable of resolving phase evolution with a time resolution of 0.1 s or less, given the rapid cooling conditions in the weld. In this regard, TRXRD with synchrotron radiation is an ideal tool.

2. Experimental

(*a*) *In situ synchrotron diffraction measurement*

TRXRD measurements were performed on the 31-pole wiggler beam line, BL 10-2 (Karpenko *et al.* 1989), at the Stanford Synchrotron Radiation Laboratory (SSRL) with the Stanford Positron–Electron Accumulation Ring (SPEAR) operating at an electron energy of 3.0 GeV and an injection current of *ca.* 100 mA.† The synchrotron white beam emerging from the 31-pole wiggler was first focused by a toroidal mirror back to the source size of *ca.* 1×2 mm, and was then monochromatized with a double Si (111) crystal. The focused monochromatic beam was then passed through a 730 μm tungsten pinhole to render a sub-millimetre beam on the sample at an incident angle

† SSRL is supported by the US Department of Energy, Division of Chemical Sciences.

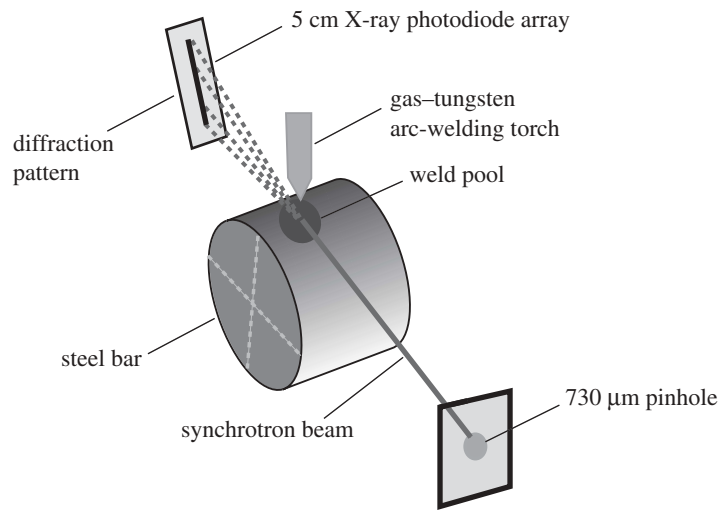

Figure 2. Schematic of the time-resolved X-ray diffraction (TRXRD) experiment for studying microstructural evolution during welding.

of *ca.* 25°. The 730 μm diameter pinhole was used to achieve the necessary time resolution in order to capture phase transformations during the rapid thermal cycling of the transient stationary welds.

This set-up yields a beam flux on the sample of 10^{10} to 10^{11} photons s^{-1}, determined experimentally using an ion chamber downstream from the pinhole. A photon energy of 12.0 keV ($\lambda = 0.1033$ nm) was chosen to maximize the number of peaks diffracting into the 2θ window, and is far enough in energy above the Fe edge to minimize the background contribution due to Fe K-fluorescence from the sample. The diffraction intensities at various 2θ positions were monitored continuously and in real time using a 50 mm long photodiode array covering a 2θ range of *ca.* 30°. In general, three BCC ferrite peaks ((110), (200) and (211)) and three FCC austenite peaks ((111), (200) and (220)) were identified.

(*b*) *Welding*

Stationary welds were produced using the gas–tungsten arc-welding process. Welding parameters are as follows: 225 A maximum direct constant current welding power supply with electrode negative polarity. A 4.7 mm diameter W-2% Th welding electrode was used and was straight-ground with a 60° included angle taper. The welding power was maintained constant at 1.9 kW (110 A, 17.5 V) for all of the welds, and current pulsing was used to help minimize the side-to-side motion of the liquid weld pool. The pulsing parameters used 130 A maximum current, 90 A background current, a maximum-to-background current ratio of 1:1 with a pulse rate of 300 pulses per second. Helium was used as the welding and shielding gas, and a cross jet of helium was used to blow the evaporated metal powders away from the area where the X-ray diffraction measurements were being taken.

The stationary welds were made by striking an arc on a stationary steel cylinder of the composition Fe–0.23 C–0.56 Mn–0.26 Si–1.77 Al–0.003 Ti–0.006 O–0.064 N (wt %). The arc was extinguished 17 s after initiation, which allowed the weld pool

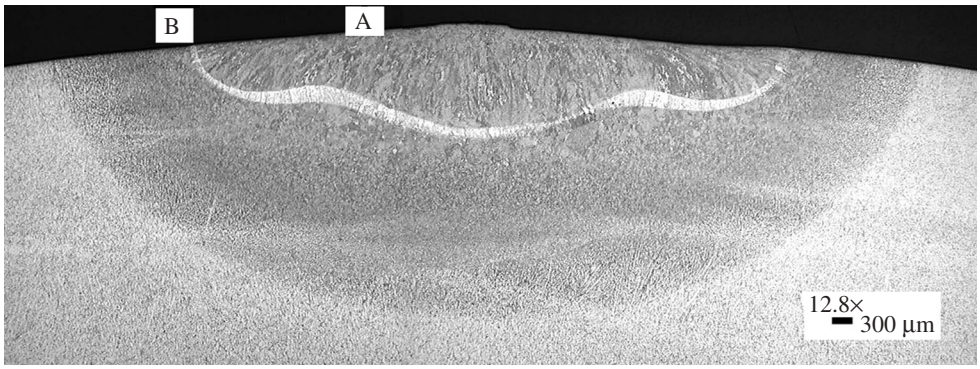

Figure 3. Macrograph of the stationary weld shows the FZ (A) and the HAZ (B) where the TRXRD measurements were made.

to achieve its maximum diameter of 9 mm. *In situ* TRXRD data were taken by positioning the beam at a fixed point within the FZ or the HAZ. TRXRD data were collected rapidly at 0.05 s intervals to observe phase transformations in real time during heating and cooling of the welds. A schematic drawing of the experimental set-up is shown in figure 2, and further details of the welding chamber, set-up and diffraction detectors are given elsewhere (Elmer *et al*. 1996, 1998; Ressler *et al*. 1998).

3. Results and discussion

A typical macrostructure of the weld produced in this experiment is shown in figure 3. The *in situ* TRXRD results from the FZ surface (marked as 'A', 2 mm from the centre of the weld) and the HAZ surface (marked as 'B', 4.5 mm from the centre of weld) are shown in figure 4. The TRXRD results of these regions are presented in two formats. First, the diffraction patterns are plotted using a time-resolved format, while in the second format, the diffraction patterns are plotted using a pseudo-colour image. The intensity ranges are given by the colour range in the image, i.e. blue represents minimum background intensity and red represents maximum intensity. The results from the HAZ are presented for a TRXRD location just adjacent to the liquid–solid interface of the stationary weld.

As soon as the arc was struck and the base metal started to heat up, the TRXRD patterns from the HAZ (see figure 4) showed a shift in the ferrite BCC (110) peaks toward lower 2θ values. These shifts are due to lattice expansion of the ferrite crystal structure, and are similar to peak shifts observed during *in situ* examinations of arc-welded titanium (Elmer *et al*. 1996, 1998; Ressler *et al*. 1998). At a time of 7 s after the arc initiation, the austenite phase was observed to form, as indicated by the appearance and increase in intensity in the FCC (111) peak. As the heating continued, the intensity of the austenite peaks continued to increase, while those of the ferrite phase decreased but never disappeared. As soon as the arc was extinguished at *ca.* 17 s, the austenite phase began to transform into ferrite, as indicated by the increase in BCC (110) peak intensity. With further cooling, the diffraction spectrum from the BCC (110) reflection shifted to higher 2θ values, indicating a decrease in lattice spacing due to the drop in temperature. Careful examination showed that some diffraction from the BCC phase was always present in addition to that of the FCC

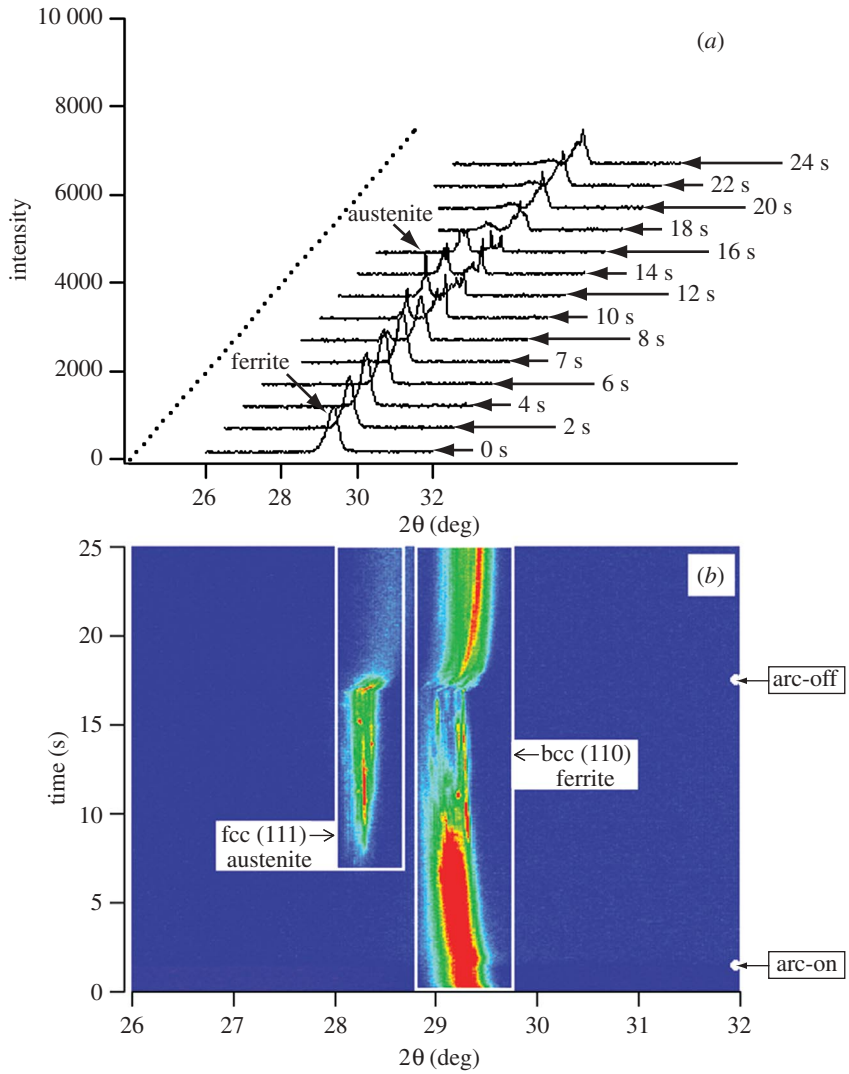

Figure 4. TRXRD results from the HAZ as a function of time for various 2θ positions. (*a*) Three-dimensional and (*b*) image representation of the data are given. The three-dimensional plots show the relative intensity; the image representation gives the details of the measurements and time resolution. The colours in the image indicate the diffracted beam intensities (red denotes strong and blue denotes background).

phase. It is important to note that this measurement was made at 4.5 mm from the weld centre, which is very close to the FZ boundary. This suggests that the ferrite and austenite may exist at the liquid–solid interface. Therefore, both ferrite and austenite are capable of growing into the liquid. This growth may occur by epitaxially from the fusion boundary during solidification. However, the phase, which ultimately becomes the primary phase to solidify in the FZ, will be determined by the growth competition between ferrite and austenite. It is possible to monitor this growth competition experimentally using TRXRD to identify the phases that solidify from the weld pool.

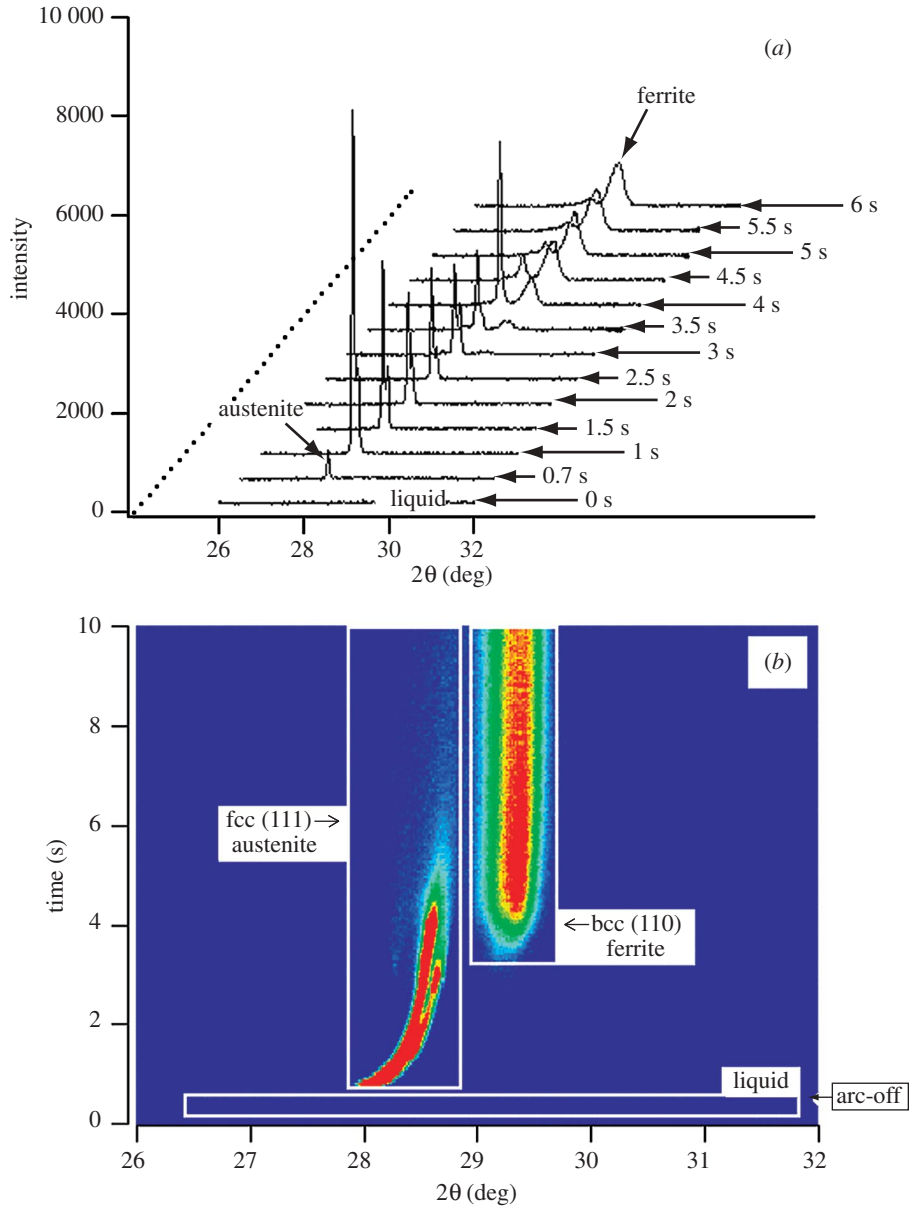

Figure 5. TRXRD results from the FZ as a function of time for various 2θ positions. (*a*) Three-dimensional and (*b*) image representation of the data are given. The three-dimensional plots show the relative intensity; the image representation gives the details of the measurements and time resolution. The colours in the image indicate the diffracted beam intensities (red denotes strong and blue denotes background).

The *in situ* diffraction results from the FZ region are shown in figure 5. While the arc was on, liquid was the only phase that was stable, as indicated by the absence of FCC and BCC diffraction peaks. After the arc was extinguished, the liquid continued to exist as the only phase for an additional 0.2 s prior to the appearance of the

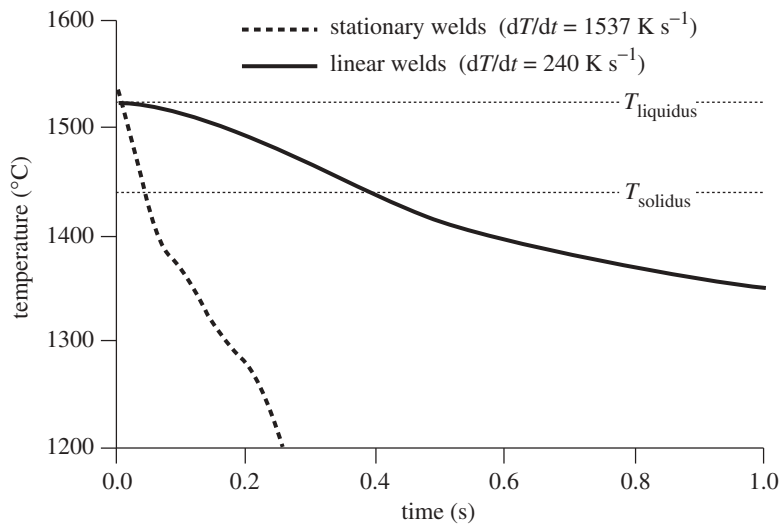

Figure 6. Comparison of temperature variations in the weld metal region of both linear and stationary welds. The plot also shows the calculated equilibrium liquidus and solidus temperatures for this steel.

austenite phase, as indicated by the FCC (111) peak. This result showed that the austenite is the primary phase to solidify from the melt under the high-cooling-rate conditions of the stationary weld, which was confirmed through additional TRXRD experiments not shown in this paper. This result is also supported by the observation of FCC (200) and FCC (220) peaks, which are not shown in figure 5. As the weld cooled, the austenite peaks shifted toward higher 2θ values, indicating a decrease in lattice spacing due to a drop in temperature. At 3 s after the onset of solidification, ferrite was observed to coexist with the austenite, as indicated by the addition of the BCC (110) peak. Upon further cooling, the ferrite peaks also shifted toward higher 2θ values as the temperature approached ambient conditions.

The TRXRD results from the FZ regions are of great significance to the welding of steels. Even in the presence of both ferrite and austenite at the fusion boundaries (see figure 4), the FZ solidified with austenite as the primary phase (see figure 5). This is in contrast to results under slower weld-cooling conditions, where solidification occurs with δ-ferrite as the primary phase (see figure 1*a*). It is important to note that the phase diagram shown in figure 1*a* does not indicate a 100% austenite phase field for the present weld compositions. Previous kinetic calculations considering diffusion in liquid, austenite and ferrite for these welds always predicted higher fractions of retained δ-ferrite at room temperature at rapid weld-cooling rates (Babu *et al.* 2001). Therefore, the present observation cannot be explained based on equilibrium thermodynamic and kinetic models.

This change in solidification mode is related to the high cooling rates experienced by the stationary welds, which were measured in a separate experiment to be 1537 K s^{-1} (see figure 6). The cooling rate in the stationary welds was experimentally measured at Lawrence Livermore National Laboratory by plunging thermocouples into the stationary weld region just before arc extinction and under the identical cooling conditions used in the TRXRD experiment. These cooling rates are 10–50

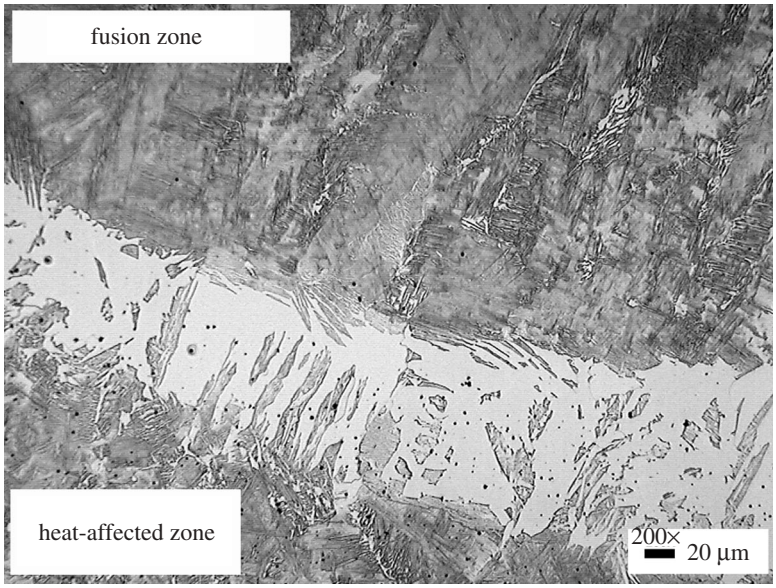

Figure 7. High-magnification optical micrograph from the weld shows the HAZ and the FZ region without the skeletal-ferrite microstructure. The FZ region contains predominantly martensite that formed from a fully austenitic phase.

times faster than those measured in a typical linear weld (M. A. Quintana & C. B. Dallam 2000, unpublished research). The cooling rates in the normal linear welds (*ca.* 240 K s^{-1}) were also measured by plunging thermocouples into the flux-cored arc welds, which yields a microstructure as shown in figure 1*a*. Because of the high cooling rates of the stationary welds, the solid–liquid boundary in these welds may be undercooled to a lower temperature. At large undercoolings, there is a competition between both δ-ferrite and austenite present in the HAZ to grow into the liquid. However, in the current research, the austenite outgrew the δ-ferrite, leading to a nearly 100% austenitic FZ microstructure prior to transforming to the low-temperature ferrite.

To confirm these TRXRD observations, the microstructure was analysed using optical microscopy (see figure 7). The metallographic results revealed a white band outlining the fusion boundary, which is predominantly δ-ferrite at room temperature (Babu *et al.* 2001), with small amounts of transformed austenite. The optical microscopy also revealed the inclusions that were originally present in the base metal. This result supports the notion that the white region is in the HAZ region. The presence of δ-ferrite and transformed austenite is in good agreement with diffraction results taken from the HAZ (see figure 4*a*), where ferrite was always observed to co-exist with austenite at high temperature. However, the microstructure in the FZ shows only the transformed austenite, i.e. martensite. The observed primary austenitic solidification mode in the FZ of this steel alloy is contrary to the expected behaviour of the primary δ-ferrite solidification suggested by equilibrium thermodynamic calculations (Babu *et al.* 2001). Understanding the welding conditions that are responsible for this critical phase transition enables a science-based approach for the design of new welding processes and consumables with optimum microstructures for industrial applications.

4. Conclusions

Formation of non-equilibrium austenite in a rapidly solidifying Fe–Al–C–Mn weld has been tracked *in situ* during rapid cooling and solidification of stationary weld nuggets. This austenite forms even with the presence of δ-ferrite in the heat-affected zone region. This mode of solidification is contrary to the formation of equilibrium δ-ferrite under normal weld-cooling conditions. This transition to non-equilibrium austenite formation is attributed to the rapid weld-cooling rate (greater than 10^3 K s^{-1}), which is higher than normal weld-cooling conditions (10^2 K s^{-1}). The present investigation demonstrated the unique capability of *in situ* TRXRD to observe phase transitions and microstructure evolution in complex multicomponent alloys subjected to rapid weld heating and cooling.

The submitted manuscript has been authored by a contractor of the US Government under contract DE-AC05-00OR22725. Accordingly, the US Government retains a non-exclusive royalty-free license to publish or reproduce the published form of this contribution, or allow others to do so, for US Government purposes.

Research sponsored by the US Department of Energy, Division of Materials Sciences and Engineering under contract no. DE-AC05-00OR22725 with UT-Battelle, LLC. A portion of this work was performed under the auspices of the US Department of Energy, Lawrence Livermore National Laboratory, under contract no. W-7405-ENG-48. The authors thank Dr C. B. Dallam of Lincoln Electric Company for allowing us to use unpublished research on cooling-rate measurements in self-shielded flux-cored arc welds.

References

Babu, S. S., David, S. A. & Quintana, M. A. 2001 Modeling microstructure evolution in self-shielded flux cored arc welds. *Weld. J.* **80**, 91s–97s.

Boettinger, W. J., Coriell, S. R., Greer, A. L., Karma, A., Kurz, W., Rappaz, M. & Trivedi, R. 2000 Solidification microstructures: recent developments, future directions. *Acta Mater.* **48**, 43–70.

David, S. A. & Vitek, J. M. 1989 Correlation between solidification parameters and weld microstructures. *Int. Metall. Rev.* **34**, 213–245.

David, S. A., Vitek, J. M. & Hebble, T. L. 1987 Effect of rapid solidification on stainless-steel weld metal microstructures and its implication on the Schaeffler diagram. *Weld. J.* **66**, 289s–300s.

Elmer, J. W., Allen, S. M. & Eager, T. W. 1989 Microstructure development during solidification of stainless-steel alloys. *Metall. Trans.* A **20**, 2117–2131.

Elmer, J. W., Wong, J., Froba, M., Waide, P. A. & Larson, E. M. 1996 Analysis of heat-affected zone phase transformations using *in situ* spatially resolved X-ray diffraction with synchrotron radiation. *Metall. Mater. Trans.* A **27**, 775–783.

Elmer, J. W., Wong, J. & Ressler, T. 1998 Spatially resolved X-ray diffraction phase mapping and $\alpha \rightarrow \beta \rightarrow \alpha$ transformation kinetics in the heat-affected zone of commercially pure titanium arc welds. *Metall. Mater. Trans.* A **29**, 2761–2773.

Fukumoto, S. & Kurz, W. 1997 The δ to γ transition in Fe–Cr–Ni alloys during laser treatment. *ISIJ Int.* **39**, 1270–1279.

Fukumoto, S. & Kurz, W. 1999 Solidification and microstructure selection maps for Fe–Cr–Ni alloys. *ISIJ Int.* **39**, 1270–1279.

Hunziker, O., Vandyoussefi, M. & Kurz, W. 1998 Phase and microstructure selection in peritectic alloys close to the limit of constitutional undercooling. *Acta Mater.* **46**, 6325–6336.

Karpenko, V., Kinney, J. H., Kulkarni, S., Neufel, K., Pope, C., Tirsell, K. G., Wong, J., Cernio, J., Troxel, T. & Yang, J. 1989 Beamline-10—a multipole wiggler beamline at SSRL. *Rev. Sci. Instrum.* **60**, 1451–1456.

Quintana, M. A., McLane, J., Babu, S. S. & David, S. A. 2001 Inclusion formation in self-shielded flux cored arc welds. *Weld. J.* **80**, 98s–105s.

Ressler, T., Wong, J. & Elmer, J. W. 1998 Investigation of real-time microstructure evolution in steep thermal gradients using *in situ* spatially resolved X-ray diffraction: a case study for Ti fusion welds. *J. Phys. Chem.* B **102**, 10 724–10 735.

Sundman, B., Jansson, B. & Andersson, J. O. 1985 The Thermo-Calc databank system. *Calphad* **9**, 1–153.

Suutala, N. 1983 Effect of solidification conditions on the solidification mode in austenitic stainless steels. *Metall. Mater. Trans.* A **14**, 191–197.